

Published in final edited form as:

Nature. 2020 November 01; 587(7835): 638–643. doi:10.1038/s41586-020-2927-z.

Host ANP32A mediates the assembly of the influenza virus replicase

Loïc Carrique^{1,5}, Haitian Fan^{2,5}, Alexander P Walker^{2,5}, Jeremy R Keown^{1,5}, Jane Sharps², Ecco Staller³, Wendy S Barclay³, Ervin Fodor^{2,6,*}, Jonathan M Grimes^{1,4,6,*}

¹Division of Structural Biology, Henry Wellcome Building for Genomic Medicine, University of Oxford, Oxford OX3 7BN, United Kingdom

²Sir William Dunn School of Pathology, University of Oxford, South Parks Road, Oxford OX1 3RE, United Kingdom

³Section of Molecular Virology, Imperial College London, St Mary's Campus, London W2 1PG, United Kingdom

⁴Diamond Light Source Ltd, Harwell Science & Innovation Campus, Didcot OX11 0DE, United Kingdom

Abstract

Aquatic birds represent a vast reservoir from which novel pandemic influenza A viruses can emerge¹. Influenza viruses contain a negative-sense segmented RNA genome which is transcribed and replicated by the viral heterotrimeric RNA polymerase (FluPol) in the context of viral ribonucleoprotein (vRNP) complexes^{2,3}. RNA polymerases of avian influenza A viruses (FluPol_A) replicate viral RNA poorly in human cells because of species-specific differences in acidic nuclear phosphoprotein 32 (ANP32), a family of essential host proteins for FluPol activity⁴. Interestingly, host adaptive mutations, particularly a glutamic acid to lysine mutation at amino acid residue 627 (E627K) in the 627 domain of the PB2 subunit (PB2₆₂₇), allow avian FluPol_A to overcome this restriction and efficiently replicate viral RNA in the presence of human ANP32 proteins. However, the molecular mechanisms of genome replication and the interplay with ANP32 proteins remain largely unknown. Here, we report cryo-EM structures of influenza C virus polymerase (FluPol_C) in complex with human and chicken ANP32A. In both structures, two FluPol_C molecules form an asymmetric dimer bridged by the N-terminal leucine-rich repeat domain (LRR) of ANP32A. The

Users may view, print, copy, and download text and data-mine the content in such documents, for the purposes of academic research, subject always to the full Conditions of use:http://www.nature.com/authors/editorial_policies/license.html#terms

* ervin.fodor@path.ox.ac.uk, jonathan@strubi.ox.ac.uk, Correspondence and requests for materials should be addressed to E.F. or J.M.G.

⁵These authors contributed equally: Loïc Carrique, Haitian Fan, Alexander Walker, Jeremy R Keown

⁶These authors jointly supervised this work: Jonathan M Grimes, Ervin Fodor

Author contributions

L.C., H.F., A.P.W., J.R.K., E.F. and J.M.G. conceived and designed the study. H.F., L.C. and J.R.K. carried out cloning of recombinant baculoviruses and protein purification, collected and processed electron microscopy data and built and refined models. A.P.W. and J.S. performed functional assays and analysed data. E.S. and W.S.B. provided plasmids and cell lines. J.M.G. and E.F. supervised the structural and functional studies, respectively. L.C., H.F., A.P.W., J.R.K., E.F. and J.M.G. wrote the manuscript, with input from all co-authors.

Competing interests

The authors declare no competing interests.

C-terminal low complexity acidic region (LCAR) of ANP32A inserts between the two juxtaposed PB2₆₂₇ domains of the asymmetric FluPolA dimer, providing insight into the mechanism behind the PB2E_{627K} adaptive mutation in mammalian hosts. We propose that this complex represents a replication platform for the viral RNA genome, in which one of the FluPol molecules acts as a replicase while the other initiates the assembly of the nascent replication product into a vRNP.

The influenza virus genome is composed of negative-sense single-stranded RNA segments (vRNA) which are assembled into separate vRNP complexes with FluPol, a heterotrimeric complex of PB1, PB2 and PA (P3 in influenza C virus) proteins, and the viral nucleoprotein (NP)^{2,3}. Following virus entry, vRNPs are trafficked to the cell nucleus where FluPol, in complex with various host factors, directs the transcription and replication of the genome⁵. For replication, FluPol first generates complementary RNA (cRNA) which then serves as template for vRNA synthesis. The molecular details of the replicase complex and, in particular, the role of the ANP32 family of host proteins, known to be essential for genome replication⁶, remain unknown. Through investigating the role of ANP32A in promoting FluPol function, we uncover a complex of ANP32A with a novel FluPol dimer which we propose acts as a replication platform for the viral genome.

ANP32A forms a complex with FluPol dimer

Host ANP32 proteins are essential for the activity of FluPol of both influenza A and B viruses^{7,8}. To address whether FluPol from influenza C virus also requires ANP32 proteins, we performed minigenome assays in human cells lacking ANP32A and ANP32B (Extended Data Fig. 1). No detectable activity was observed in the double knockout cells but expression of human ANP32A (huANP32A), human ANP32B (huANP32B) or chicken ANP32A (chANP32A) restored FluPol_C activity. We then used cryo-EM to solve the structures of FluPol_C in complex with huANP32A and chANP32A at a resolution ranging from 3.0 to 3.6 Å, respectively (Fig. 1a, b, Extended Data Fig. 2 and 3, Extended Data Table 1, Supplementary Video 1). In these structures, two heterotrimeric FluPol_C molecules assemble into an asymmetric dimer with the N-terminal leucine-rich repeat domain of ANP32A (ANP32A_{LRR})⁹ bridging the two FluPol_C molecules. The C-terminal low complexity acidic region of ANP32A (ANP32A_{LCAR}) could not be fully resolved in the structures. The two structures of FluPol_C dimers with huANP32A and chANP32A are largely identical, showing the same FluPol_CFluPol_C and FluPol_C-ANP32A_{LRR} interaction interfaces. About 22% of particles in the FluPol_C.chANP32A dataset lack density for ANP32A and were used to reconstruct a 3.4 Å resolution polymerase-only structure which shows the same arrangement of FluPol_C dimer as the ANP32A-containing complexes (Fig 1c, Extended Data Fig. 2 and 3, Extended Data Table 1).

FluPol forms an asymmetric dimer

The first FluPol molecule (hereafter designated as the FluPol replicase, FluPol^R) is fully resolved in the density map and shows a configuration of the peripheral flexible domains distinct from that in the cap-snatching competent transcriptase, but similar to that previously observed for RNA-free FluPol and FluPol bound to complementary RNA (cRNA)^{10,11} (Fig. 1, Extended Data Fig. 4, Supplementary Video 1). Specifically, the cap-binding domain of

PB2 (PB2_{cap}) is immobilized through extensive contacts with the palm subdomain of PB1 while the nuclear localization signal (NLS) domain of PB2 (PB2_{NLS}) intimately associates with the N-terminal endonuclease domain of P3 (P3_{endo}). The 627 domain of PB2 (PB2₆₂₇), named after host-specific amino acid residue 627, makes relatively few contacts with the rest of FluPol^R. FluPol^R is bound to a 47 nucleotide long vRNA, whose 5' terminus is clearly resolved and shows the typical hook structure bound in a pocket formed by P3 and PB1, as observed previously^{12,13} (Fig. 1; Extended Data Fig. 5). In the majority of particles, the 3' vRNA terminus cannot be resolved, but density observed around the template entry channel suggests that it has entered the active site. In ~10% of FluPol_C-chANP32A and ~7% of FluPol_C-huANP32A particles the 3' vRNA terminus is bound at the interface of the C-terminal domain of P3, the thumb subdomain of PB1 and the N1 subdomain of PB2, as recently described for FluPol_A and FluPol_D^{12,14,15}. The second FluPol molecule (hereafter designated as the encapsidating FluPol, FluPol^E) shows a dramatically different configuration of the flexible domains which has not been seen previously. Most strikingly, the C-terminal flexible domains of PB2 (PB2_{cap}, PB2_{mid-link}, PB2₆₂₇ and PB2_{NLS}) flip over to pack against the C-terminal domain of the P3 subunit (P3_{CTD}) (Extended Data Fig. 4, Supplementary Video 1). P3_{endo}, several N-terminal domains of PB2, and the C-terminal 18 amino acid residues of PB2_{NLS} are disordered in FluPol^E. Furthermore, ~52% of FluPol_C-chANP32A and all FluPol_C-huANP32A particles lack the density for PB2_{cap} and PB2_{mid-link} in FluPol^E, suggesting the flexibility of these domains. No RNA was found associated with FluPol^E. The two FluPol_C molecules make extensive interactions, mainly between their respective PB2 and P3 subunits, to form a large polymerase dimer interface burying a total of ~1,500 Å² (Fig. 2a). The PB2₆₂₇ domain of FluPol^R interacts with the P3_{CTD}, PB2₆₂₇ and PB2_{NLS} domains of FluPol^E (Fig. 2b), and the P3_{CTD} domain of FluPol^E stacks against the PB2 N2 (PB2_{N2}) and PB2_{mid-link} domains of FluPol^R (Fig. 2c). In addition, the P3 arch and PB1 β-hairpin of FluPol^E contact the P3_{CTD} and PB2_{N2} domains of FluPol^R (Fig. 2d). This dimer interface is distinct from that observed previously in FluPol_A, which is required for replication initiation on a cRNA template by promoting template realignment^{12,16}. To address the functional relevance of this novel dimer interface in influenza A virus, we introduced alanine mutations to several clusters of amino acid residues in FluPol_A located at or close to the dimer interface based on the structure of the FluPol_C heterotrimeric dimer. These include the residues PA K324/H326/E327, PA K339/Q340, and PB2 P132, which are structurally equivalent to P3 R299/K301/D302, P3 N318/Q319, and PB2 E139 in FluPol_C, respectively (Supplementary Fig. 1). All these mutations resulted in a reduction of viral RNA levels in a minigenome assay analysing FluPol function (Extended Data Fig. 6a). These data indicate that amino acid residues at the asymmetric FluPol dimer interface we have identified in the FluPol_C-ANP32A complexes are important for FluPol activity.

ANP32A_{LRR} bridges the asymmetric FluPol dimer

In both the FluPol_C-huANP32A and FluPol_C-chANP32A structures, the ANP32A_{LRR} domain binds in a depression formed by the FluPol_C dimer interface (Fig. 1a, b; Fig 2e, Supplementary Video 1). The N-terminal region of ANP32A_{LRR} interacts with FluPol^R, involving multiple regions of PB2 that include the lid domain (PB2_{lid}), PB2₆₂₇ and PB2_{NLS}

(Fig. 2e, f). These interactions bury a total of $\sim 600 \text{ \AA}^2$ at the interface between ANP32A and FluPol^R. The C-terminal region of ANP32A_{LRR} interacts with the P3_{CTD} domain and the N-terminus of PB1 of FluPol^E, and buries a total of $\sim 490 \text{ \AA}^2$ at the interface (Fig. 2e, g, h). Two amino acid residues in ANP32A, N129 and D130, previously identified as important for FluPol_A binding and activity^{8,17}, are directly involved in the interaction with FluPol^E. Specifically, N129 is sandwiched between M387 and K391 of P3 and interacts with K391 directly through hydrogen bonding, while D130 interacts with K608 of P3 (Fig. 2g). To address the functional relevance of this interaction we mutated PA K413 in FluPol_A, equivalent to P3 K391 in FluPol_C (Fig. 2g, Supplementary Fig. 1), to alanine. This mutant FluPol_A showed reduced binding to huANP32A and loss of activity in a minigenome assay (Extended Data Fig. 7). Further mutations in FluPol_A at PA D529 and PB2 T609, corresponding to P3 E513 and PB2 H631 in FluPol_C (Fig. 2f, g, Supplementary Fig. 1), had similar inhibitory effects on both ANP32A binding and FluPol activity. Taken together, these data confirm the functional relevance of the identified ANP32A-FluPol interaction and provide an explanation for why chANP32B with I129 and N130 is unable to support FluPol activity^{8,17}.

ANP32A_{LCAR} interacts with PB2₆₂₇

Species-specific differences in ANP32 proteins underpin the poor activity of avian FluPol_A in mammalian cells⁴. Amino acid differences important for FluPol activity have been identified in both ANP32A_{LRR} and ANP32A_{LCAR}, but a 33 amino acid insertion in the avian ANP32A_{LCAR} when compared to mammalian ANP32A_{LCAR} was found to be the most critical for the ability of avian ANP32A to support the activity of avian FluPol_A^{4,18,19} (Fig. 3a). Although the ANP32A_{LCAR} could not be built unambiguously in the map, continuous density shows that it contacts PB2₆₂₇ of FluPol^R (Fig. 3b, c, Supplementary Video 2). These data are in agreement with previous reports of a direct interaction between ANP32A and the PB2₆₂₇ domain using biochemical and NMR methods^{20–22}. In the FluPol_C-chANP32A structure, the negatively charged chANP32A_{LCAR} binds in a basic groove formed by the PB2₆₂₇ domains of FluPol^R and FluPol^E, with the avian-specific 33 amino acid insertion directly contacting the PB2₆₂₇ domain of FluPol^R. This interaction positions a previously identified hydrophobic SUMO interaction motif (SIM)-like sequence²³ (Extended Data Fig. 1c) on top of PB2₆₂₇, as well as a downstream region of the ANP32_{LCAR} which contains a mixture of basic and acidic amino acid residues (176-VLSLVKDR-183) (Fig. 3a-c). Specifically, this motif is located next to PB2 K649 (equivalent to E627 in the PB2 of avian FluPol_A) and V614. PB2 V614 is equivalent to K591 in the swine origin 2009 H1N1 pandemic influenza A virus, which retained E627 in its avian PB2 but used a Q591K adaptation to increase polymerase activity^{24,25} (Extended Data Fig. 8 and Supplementary Fig. 1). Interaction of this region of ANP32A with PB2₆₂₇ could be critical for stabilization of the interaction between ANP32A and FluPol and, consequently, for the ability of ANP32A to support FluPol activity. The presence of a mixture of basic and acidic amino acid residues in this region could explain why avian ANP32A is able to support FluPol with either avian-specific 627E or mammalian-specific 627K in PB2. The corresponding region in huANP32A (176-EEEYDEDA-183), as well as in the huANP32B isoform (176-DEEDEDDE-183), is entirely acidic (Fig. 3a), potentially

explaining the need to eliminate the acidic 627 amino acid residue in avian FluPol_A upon viral transmission to a mammalian host. To test this hypothesis, we replaced the acidic 176-183 region of huANP32A with the corresponding region from chANP32A and found that this mutant form of huANP32A was able to fully support the activity of FluPol_A with 627E in mammalian cells (Fig. 3d). These data are also in agreement with a previous study reporting that FluPol_A can tolerate a range of non-acidic amino acid residues at position 627 and activity is positively correlated with the pI value of the amino acid²⁶. Thus, our data provide an explanation for adaptive mutations observed in FluPol_A upon transmission of influenza A virus from an avian to a human host.

Implications for genome replication

The product exit channel of FluPol^R, located along the PB1 finger domains and PB2_{cap}, points towards the 5' vRNA binding site of FluPol^E which is located next to the PA arch (343-376) and the PB1 β-hairpin (353-370)^{13,15}. A path lined with basic amino acid residues connects the exit channel with the 5' vRNA binding site and could facilitate the transfer of the nascent RNA product from FluPol^R to FluPol^E (Fig. 4a, Supplementary Video 3). FluPol^E is thus ideally positioned to capture the 5' end of a nascent RNA product emerging from the active site of FluPol^R. This suggests that in the FluPol_C-ANP32A complex, FluPol^R functions as the replicase whilst FluPol^E acts as an 'encapsidating' polymerase, initiating the co-replicative assembly of the nascent RNA with nucleoprotein (NP) into an RNP. To test this hypothesis, we performed a cRNA stabilisation assay²⁷ to examine the ability of FluPol to encapsidate nascent RNA product. Mutations in FluPol^E at positions PA K324/H326/E327 and PA K339/Q340 caused a significant reduction in cRNA accumulation. Note that PB2 P132 is located on the FluPol^R side of the interface and therefore this mutation could not be tested using this assay. These data confirm that the FluPol^R-FluPol^E interface is important for encapsidation of a nascent cRNA product (Extended Data Fig. 6b). Furthermore, the PB2₆₂₇ domain of FluPol^E has been implicated in cRNA encapsidation using this assay, which is consistent with our model²⁸. We propose that a similar mechanism is likely to apply for cRNA-bound FluPol^R, due to intrinsic similarities between cRNA synthesis and vRNA synthesis, both requiring co-replicative encapsidation of nascent RNA.

Such a role for the FluPol-ANP32A complex in viral genome replication is consistent with previous observations; in particular, ANP32A and the adaptive PB2 E627K mutation have been specifically linked to viral genome replication rather than transcription^{7,29,30} providing strong support for a role of the FluPol-ANP32A complex in the former process. We were unable to fully resolve the ANP32A_{LCAR} in our structures, indicating that this part of ANP32A is highly dynamic. Replication involves viral NP that co-replicatively coats viral RNA along its length, but it is currently unknown how NP is recruited onto the growing nascent chain of RNA. Nonsegmented negative-strand RNA viruses encode an acidic phosphoprotein (P) that is an essential component of their RNA polymerase complex and is involved in recruiting NP to nascent replication product³¹. Segmented negative-strand RNA viruses do not encode an equivalent protein and it is tempting to speculate that instead they hijack a cellular protein like ANP32A to fulfil such function. Specifically, the unstructured region of ANP32A_{LCAR}, downstream of the region interacting with FluPol^R, could act as a

molecular whip recruiting NP in a manner analogous to that proposed for the P phosphoprotein.

Understanding the structural basis of why ANP32A is fundamental to influenza virus replication opens a new perspective on the role of ANP32A and host adaptive mutations in FluPol function. Specifically, our data suggest that the FluPol-ANP32A complex represents a replication platform for the influenza virus RNA genome. The mechanistic insights gained have allowed us to build a more complete picture of the structural basis for the viral replication cycle. During infection, incoming vRNPs will bind to the C-terminal domain of host RNA polymerase II through interactions primarily mediated by the PA_{CTD} of FluPol^{32,33}. This interaction stabilizes FluPol in a cap snatching-competent conformation, allowing the cleavage of host capped RNAs which serve as primers for the initiation of viral mRNA synthesis³³. Accumulation of newly synthesised FluPol will favour genome replication over transcription, consistent with a transition from transcription to replication as infection proceeds, through forming an asymmetric dimer with the RNP-associated resident FluPol and stabilising it in a replication-competent conformation allowing primer-independent replication initiation (Fig. 4). ANP32A contributes to the stabilisation of this dimer by bridging the two FluPol molecules. Several lines of evidence suggest that ANP32A is involved in cRNA to vRNA replication although there is also evidence in favour of a role during vRNA to cRNA replication^{7,18,29,30}. In particular, avian polymerase in human cells is incapable of generating replication competent cRNPs, suggesting that cRNA encapsidation and hence the correct assembly of cRNPs might be affected²⁹; this is fully consistent with our data showing that mutations at the FluPol^RFluPol^E dimer interface interfere with cRNA encapsidation. ANP32A may play a particularly important role in stabilizing the interaction of a free FluPol with a cRNP-associated FluPol, as cRNPs need to make at least two different interactions with free FluPol molecules using two different interaction interfaces, to promote template realignment and nascent product encapsidation. These interactions need to be fine-tuned in a host-dependent manner in agreement with the observation of adaptive mutations at the dimer interfaces^{12,34}. Dependence on free FluPol to ensure template realignment during replication initiation on a cRNA template¹², and co-replicative genome assembly into an RNP, both provide the virus with a safety mechanism to avoid the generation of naked viral RNA in the absence of viral protein synthesis, which could otherwise be a trigger for activating innate immune responses³⁵. The identification of amino acid residues involved in mediating ANP32A-FluPol interactions will facilitate both the development of novel small molecule inhibitors that disrupt the interaction interface and the design of genetically engineered animals resilient to influenza virus.

Methods

No statistical methods were used to predetermine sample size. The experiments were not randomized and investigators were not blinded to allocation during experiments and outcome assessment.

Cells

Human embryonic kidney 293T (HEK-293T) and Sf9 insect cells were sourced from the Cell Bank of the Sir William Dunn School of Pathology, University of Oxford. HEK-293T cells were maintained in Dulbecco's Modified Eagle Medium (DMEM) and Sf9 cells were maintained in Sf-900 II serum free medium (Gibco). Human eHAP cells, control or lacking ANP32A and ANP32B proteins (dKO), were cultured in Iscove's modified Dulbecco's medium (IMDM; Sigma) supplemented with 10% foetal bovine serum (FBS; Sigma), 1% nonessential amino acids (NEAA; Gibco), and 1% penicillin/streptomycin (Gibco) and have been described⁷. Cell lines have not been authenticated but tested negative for mycoplasma contamination.

Protein expression and purification

The three subunits of influenza C/Johannesburg/1/1966 virus polymerase, together with human or chicken ANP32A, were co-expressed in Sf9 cells from codon-optimized genes (GeneArt) cloned into a single baculovirus using the MultiBac system³⁶. Expression and purification of the co-expressed complex were performed as previously described^{10,12} with minor modifications: the salt concentration in all buffers was set to 150 mM to maintain FluPol_C-ANP32A complex formation. Size exclusion chromatography (SEC) was performed using 25 mM HEPES-NaOH, pH 7.5, 150 mM NaCl and 5% (v/v) glycerol on a Superdex 200 Increase 10/300 GL column (GE Healthcare).

Cryo-EM sample preparation

Protein surface charges of the purified complex were neutralized by adding 0.001% glutaraldehyde for 20 min on ice to minimize preferential orientation of particles. After quenching the reaction by adding Tris-HCl, pH 8.0 to a final concentration of 100 mM, the sample was injected onto a Superdex 200 Increase 10/300 GL column (GE Healthcare) together with a 47 nt vRNA (5'-AGUAGAAACAAGGGUAUUUUUCUUUACUAGUCUACCCUGCUUUUGCU-3') using 25 mM HEPES-NaOH, pH 7.5, 150 mM NaCl as the running buffer. This 47 nt vRNA contains the 5' and 3' promoter elements recognised and bound by FluPol. The fractions of interest were concentrated to 0.23–0.28 mg ml⁻¹ and RNA binding was confirmed by measuring the A260/A280 ratio. A final concentration of 0.005% (v/v) Tween 20 was added before grid preparation. A volume of 3–4 µl of sample was placed on glow-discharged Quantifoil Holey Carbon grids (R 2/1, with 2 µm holes and 1 µm spacing and applied on biocompatible 200 gold mesh), before blotting for 3.0–3.5 sec and flash-freezing in liquid ethane. All grids were prepared using a Vitrobot mark IV (FEI) at 95–100% humidity.

Cryo-EM image collection and processing

Cryo-EM data for the FluPol_C-chANP32A sample were collected on a 300 kV Titan Krios microscope (Thermo Fisher Scientific) at the Division of Structural Biology (Strubi). Automated data collection was setup in EPU 2.1 using a K2 Summit (Gatan) direct electron detector at 1.37 Å per pixel operating in counting mode and a GIF Quantum energy filter (Gatan) with 20 eV slit. Sample was collected with a tilt angle of 30° at a dose of ~38.8 e-/Å² across 44 frames for a dose rate of ~3.527 e-/Å²/sec, using a defocus range of -2 µm to

-3.5 μm . Cryo-EM data for the FluPol_C-huANP32A sample were collected on a 300 kV Titan Krios microscope (Thermo Fisher Scientific) at Electron Bio-Imaging Centre (eBIC). Automated data collection was setup in SerialEM 3.7 using a K3 (Gatan) direct electron detector operating in super-resolution mode at 0.5425 \AA per pixel and a GIF Quantum energy filter (Gatan) with 20 eV slit. Sample was collected with a tilt angle of 20° at a dose of $\sim 32.1 \text{ e}^-/\text{\AA}^2$ across 34 frames for a dose rate of $\sim 16 \text{ e}^-/\text{\AA}^2/\text{sec}$, using a defocus range of -2 μm to -3.5 μm . Sample-specific data collection parameters are summarized in Extended Data Table 1. Data processing pipelines are shown in Extended Data Fig. 1. Briefly, raw movies were processed using MotionCor2-1.1.0³⁷, with a five-by-five patch-based alignment, keeping all the frames and dose-weighting up to the total exposure. For the K3 super-resolution, the data have been binned 2 times at the motion correction step, giving a final pixel size of 1.085 \AA per pixel. The contrast transfer function (CTF) of full-dose, non-weighted micrographs was initially estimated using Gctf-v.1.06³⁸ or cryoSPARC v.2.12.0³⁹ Patch-CTF. Poor-quality images were discarded after manual inspection. Particles were blob picked in cryoSPARC v.2.12.0³⁹ and the 2D classes were inspected and classes of interest were selected to generate templates for complete particle picking. For the FluPol_C-chANP32A dataset, a total number of 2,312,045 particles were picked and a final number of 772,989 particles were exported to RELION 3.1⁴⁰ after 2D/3D class selection. The consensus map was refined to 3.50 \AA . Bayesian polishing and per particle CTF refinement and B-factor estimation with beam tilt correction were performed in RELION 3.1 which improved map resolution to 3.2 \AA . High order aberration and Magnification Anisotropy refinement improved map resolution to 3.1 \AA . Global and focus 3D classification were performed within RELION (Extended Data Fig. 2a). For the 3D variability analysis, polished particles and model were imported into cryoSPARC v.2.12.0 and refined using the non-uniform refinement job. A mask was then designed around the density corresponding to the PB2₆₂₇ domains of both polymerases and chANP32A. The 3D variability analysis was then performed using this mask, asking for solving the three main modes on a structure low pass filtered to 6 \AA . The results of this principal component analysis (PCA) were clustered in twenty sub-populations and models were reconstructed for each of the individual clusters. One cluster was showing a clear density for the chANP32A_{L_CAR} region and was refined using the non-uniform refinement job to 3.6 \AA (Subclass 2). In parallel, all the particles having a strong density for chANP32A were selected and refined using the nonuniform refinement job to 3.1 \AA . The same 3D variability analysis was performed, asking for solving the three main modes on a structure low pass filtered to 6 \AA . Mode 3 is displayed as Supplementary Video 2. For the FluPol_C-huANP32A data set, a total number of 2,534,332 particles were picked and a final number of 970,198 particles were exported to RELION 3.1 after 2D/3D class selection. The consensus map was refined to 3.2 \AA . Bayesian polishing and per particle CTF refinement and B-factor estimation with beam tilt correction were performed in RELION 3.1 which improved map resolution to 2.8 \AA . Global and focus 3D classification were performed within RELION (Extended Data Fig. 2b). CryoEF⁴¹ and 3D FSC⁴² sphericity scores were used to confirm that the final maps were not suffering from distortion bias due to preferred specimen orientation. The structures were modelled by first fitting the ANP32A LRR domain (PDB ID: 4XOS), FluPol_C (PDB ID: 5D98) and 5'3' vRNA (PDB ID: 6RR7) using UCSF Chimera⁴³. One cycle of rigid body real space refinement followed by manual adjustment in Coot⁴⁴ was performed to correctly position the

C α chain into the density. Locally sharpened maps were generated using LocScale⁴⁵ through the CCP-EM⁴⁶ package. Finally, cycles of PHENIX⁴⁷ real space refinement and manual building in Coot⁴⁴ were used to improve model geometry. Map-to-model comparison in PHENIX mtriage validated that no over-fitting was present in the structures. Model geometry was validated for all models using MolProbity⁴⁸. All map and model statistics are detailed in Extended Data Table 1. A homology model of FluPol_A-ANP32A complex structure was generated using SWISS-MODEL⁴⁹.

Plasmids

Plasmids pHMG-PB1, pHMG-PB2, pHMG-P3 and pHMG-NP expressing the subunits of FluPol_C and NP of influenza C/Johannesburg/1/66 virus and pPolI-Luci-CP3-RT expressing a luciferase reporter have been described^{50,51}. pcDNA-PB1, pcDNA-PB1a (catalytically inactive; D445A/D446A), pcDNA-PB2, pcDNA-PB2 K627E, pcDNA-PA, pcDNA-NP and pPOLI-NA, which encodes an NA vRNA segment, are derived from influenza A/WSN/33 virus and have been described previously^{27,52-54}. pCAGGS-chANP32A has been described previously⁴. pcDNA-huANP32A and pCAGGS-huANP32A-Strep were produced from pCAGGS-huANP32A⁴ by restriction-ligation cloning. pcDNA-huANP32A 176-183, pcDNA-PB2 T609A, pcDNA-PB2 P132A, pcDNA-PA D529A/R531A/E533A, pcDNA-PA K413A, pcDNA-PA K324A/H326A/E327A and pcDNA-PA K339A/Q340A were generated from pcDNA-huANP32A, pcDNA-PB2 and pcDNA-PA by site-directed PCR mutagenesis and validated by Sanger sequencing.

Influenza C virus RNP reconstitution and luciferase reporter assays

Approximately 0.2×10^6 eHAP cells, control or dKO, were transfected with plasmids pHMG-PB1, pHMG-PB2, pHMG-P3, pHMG-NP, pPolI-Luci-CP3-RT and pcDNA-Renilla using Lipofectamine 2000 according to manufacturer's instructions. Where indicated, plasmids pCAGGS-huANP32A, pCAGGS-huANP32B or pCAGGS-chANP32A were included. Cells were lysed 24 hours post-transfection using Passive lysis buffer (Promega). Firefly and Renilla luciferase activities were measured using a Promega dual luciferase kit and firefly activity levels were normalised to the Renilla control.

Influenza A virus RNP reconstitution assay and primer extension analysis

Approximately 0.2×10^6 HEK 293T cells were transfected with plasmids pcDNA-PB1, pcDNA-PB2, pcDNAPA, pcDNA-NP and pPOLI-NA using Lipofectamine 2000 according to manufacturer's instructions. Where indicated, plasmids encoding ANP32A proteins or mutant polymerase subunits were included. Total cellular RNA was extracted 20 hours post-transfection using TRI reagent (Sigma) according to the manufacturer's instructions. NA segment RNA levels were assessed using primer extension⁵⁵. Briefly, primers complementary to the positive (5'-TGGACTAGTGGGAGCATCAT-3') and negative (5'-TCCAGTATGGTTTTGATTCCG-3') sense NA segment viral RNA species were labelled with ³²P and total cellular RNA was reverse transcribed. A primer complementary to 5S rRNA (5'-TCCCAGGCGGTCTCCCATCC-3') was included as a loading control. Products were resolved by 6% denaturing PAGE and visualised by phosphorimaging. Product bands were identified by comparison with previously published data^{56,57}. Analysis was carried out

using ImageJ⁵⁸ and Prism 8 (GraphPad), and viral RNA signals were normalised to the 5S rRNA loading control.

Western blotting

Western blotting of all proteins was carried out using specific rabbit polyclonal antibodies. PB1 and PB2 were blotted using commercially available antibodies (Genetex), while PA was blotted using a custom-made antibody⁵⁹. ANP32A and actin were blotted using commercially available antibodies (Sigma). In all cases the secondary antibody used was goat anti-rabbit conjugated to HRP, and Amersham ECL Western Blotting Detection Reagents (GE) were used for detection.

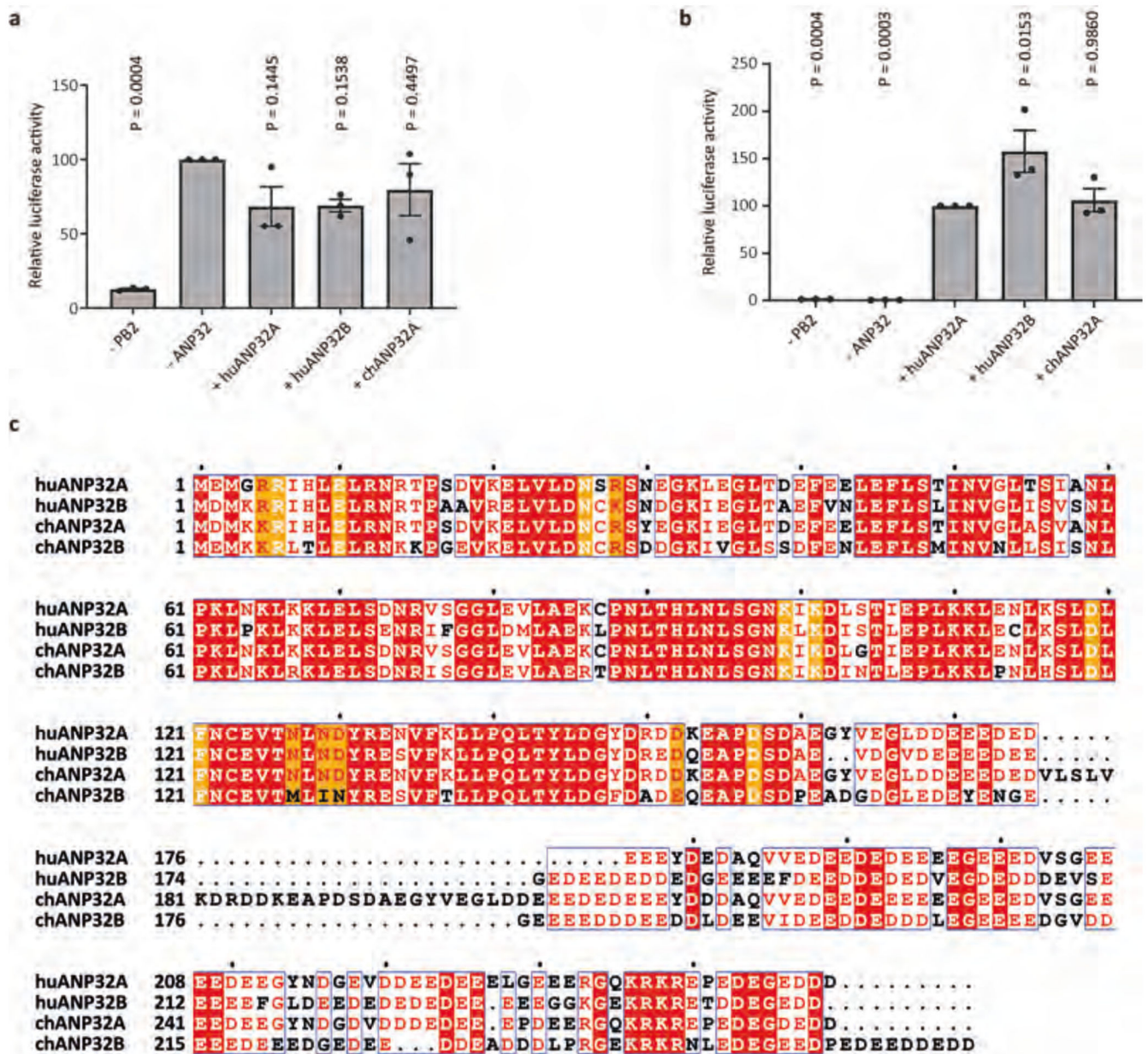
Affinity purification assays

Approximately 2×10^6 HEK 293T cells were transfected with pcDNA-PB1, pcDNA-PB2, pcDNA-PA and pCAGGS-huANP32A-Strep. 48 hours post-transfection, cells were lysed in 500 μ l of lysis buffer (50 mM Tris-HCl pH 8.0, 200 mM NaCl, 25% glycerol, 0.5% Igepal CA-630, 1 mM DTT, 1 mM PMSF, 1 x complete EDTA-free protease inhibitor cocktail tablet (Roche)) for 1 hr at 4 °C and cellular debris was cleared by centrifugation for 5 min at 17000 x g. The supernatant was diluted in 2 ml 150 mM NaCl and incubated with Strep-Tactin beads (IBA) for 2 hr at 4 °C. Beads were washed 3 x in wash buffer (10 mM Tris-HCl pH 8.0, 150 mM NaCl, 10% glycerol, 0.1% Igepal CA-630, 1 mM PMSF) and complexes were eluted in 1 x Buffer E (IBA) Strep-Tactin elution buffer for 16 hr at 4 °C. Eluted complexes were analysed by 12% SDS PAGE and western blotting.

cRNA encapsidation assays

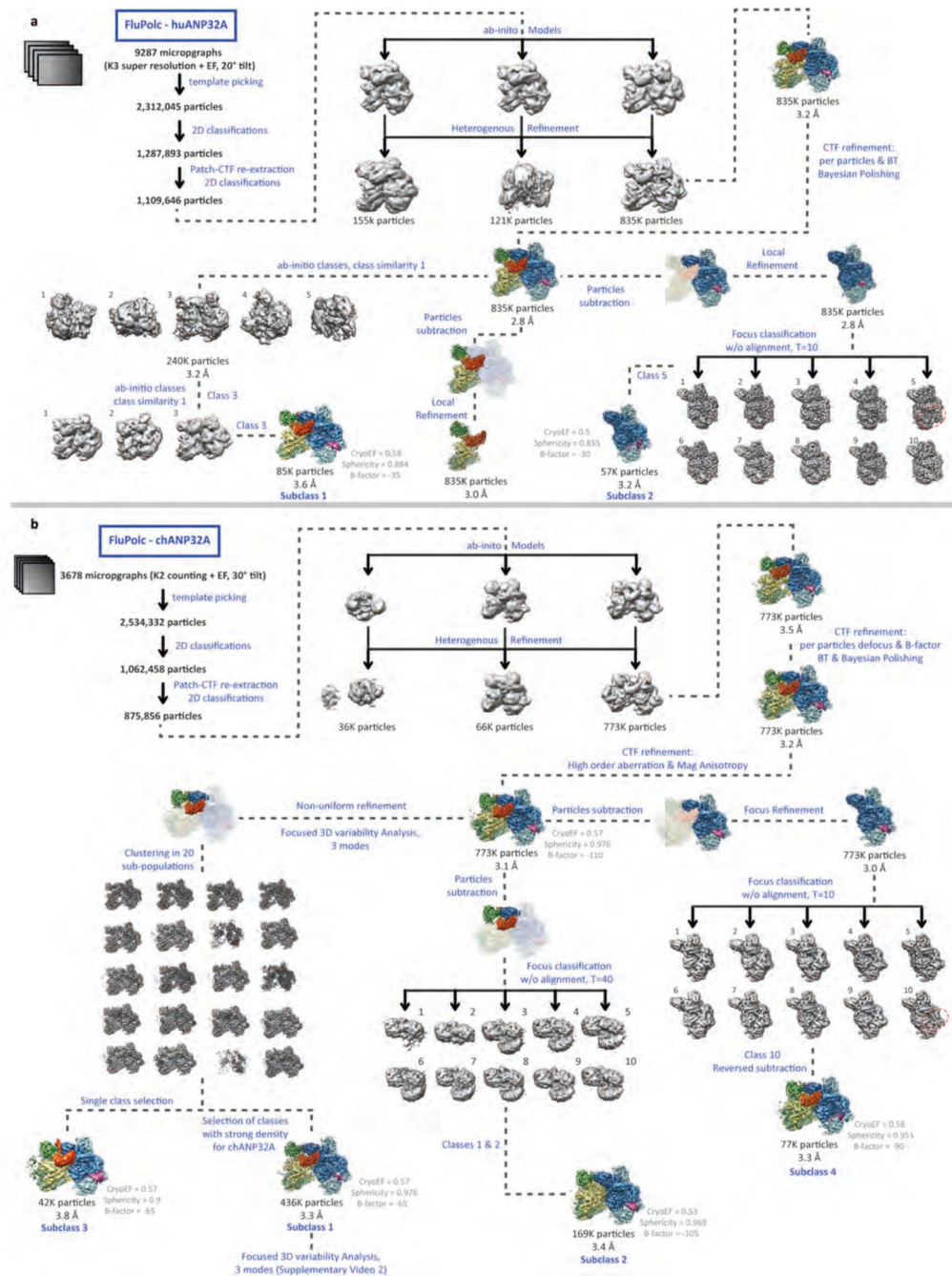
cRNA encapsidation assays were performed as described previously²⁷. In brief, approximately 1×10^6 HEK 293T cells were transfected with pcDNAPB1a, pcDNA-PB2, pcDNA-PA and pcDNA-NP using Lipofectamine 2000 according to the manufacturer's instructions. 48 hours post-transfection, culture media was replaced with DMEM containing 0.5% FBS and 5 μ g/mL actinomycin D and influenza A/WSN/33 virus at multiplicity of infection 5.0. Total cellular RNA was extracted 6 hours post-infection using Trizol (Sigma) according to the manufacturer's instructions, and viral RNA levels were determined by primer extension analysis as described above.

Extended Data



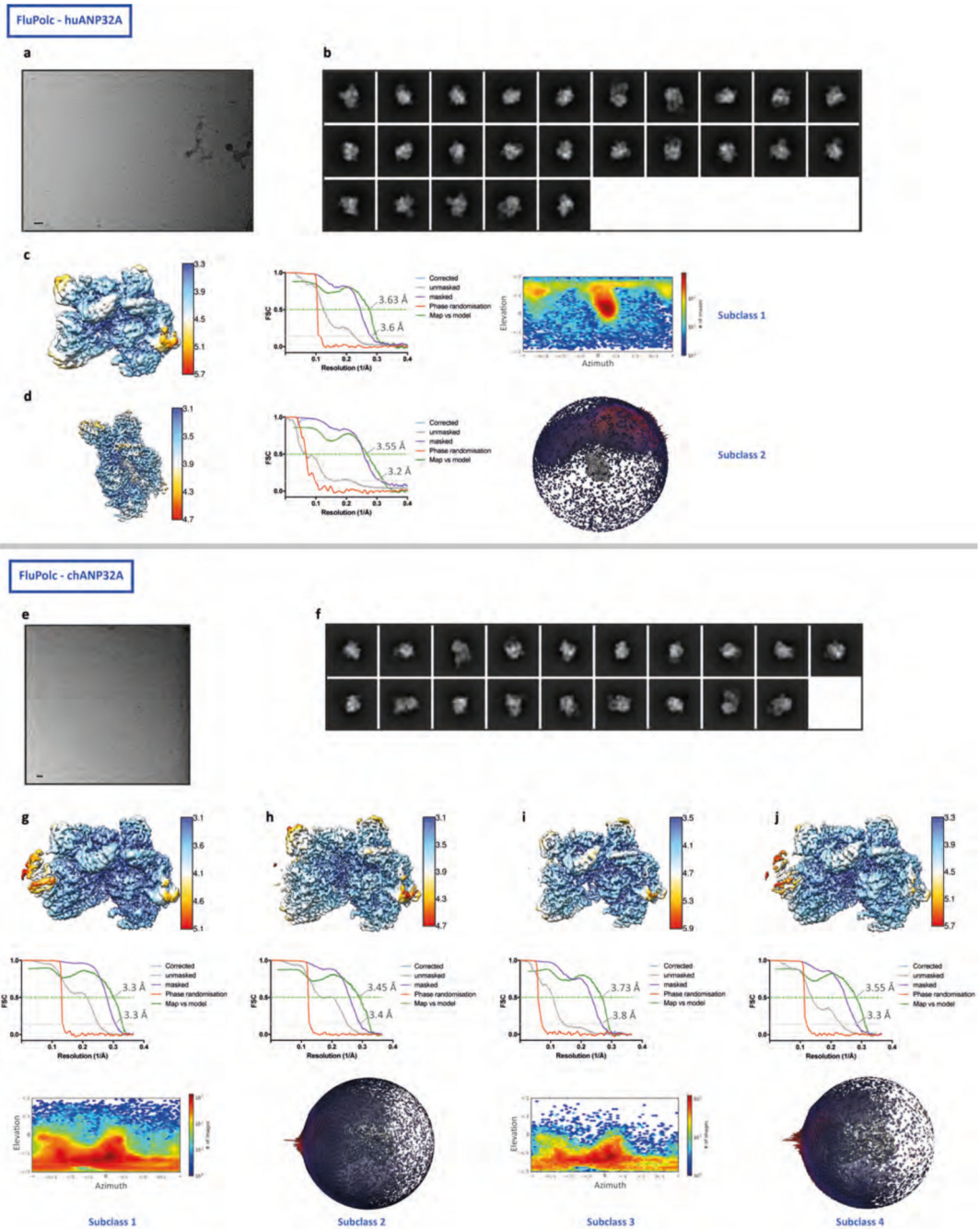
Extended Data Fig. 1. FluPol_C activity depends on ANP32A and alignment of ANP32 proteins. **a, b**, Luciferase reporter gene activities reflecting FluPol_C activity in control (**a**) and dKO (**b**) eHAP cells in the presence or absence of overexpressed huANP32A, huANP32B or chANP32A. Data are presented as mean values \pm s.e.m. $n = 3$ biologically independent samples from $n = 3$ independent experiments. Ordinary one-way ANOVA with Dunnett's post hoc test for multiple comparisons. $P < 0.05$ is considered significant to reject the null hypothesis. **c**, Sequence alignment of huANP32A, huANP32B, chANP32A, chANP32B. Residues involved in hydrogen bonding interactions with FluPol_C are indicated in orange. The chANP32A avian-specific 33 amino acid insertion is highlighted in cyan. The SUMO

interaction motif (SIM) sequence is indicated by black triangles. The figure was prepared with Esprint 3.0⁶⁰.



Extended Data Fig. 2. Data collection, processing and analysis scheme.

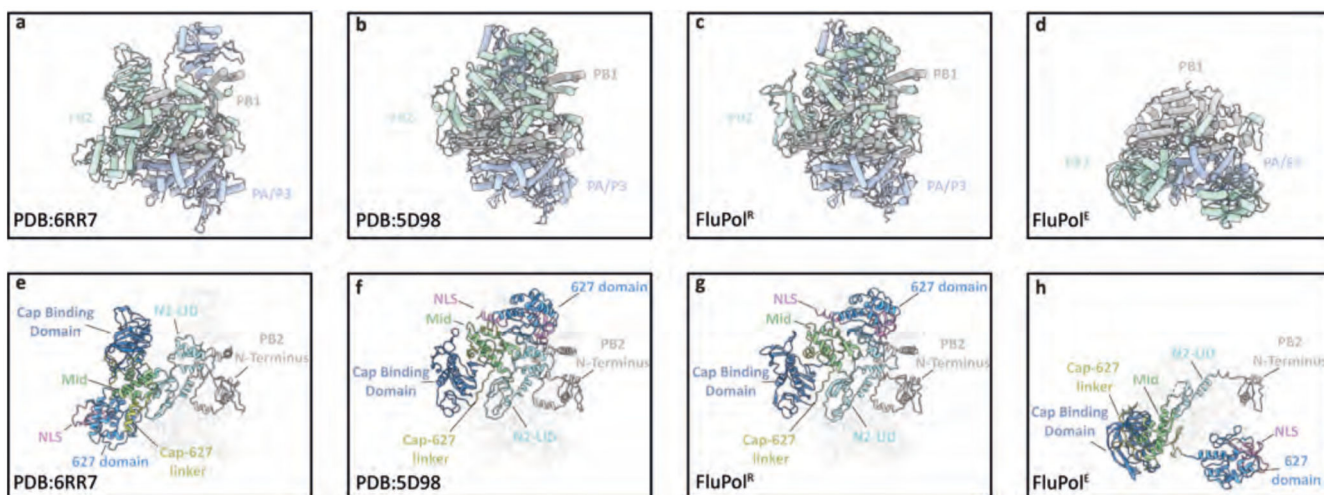
a, b, Flowchart for the processing and the classification of the FluPol_C-huANP32A complex (**a**) and FluPol_C.chANP32A complex (**b**).



Extended Data Fig. 3. Single-particle cryo-EM analysis of FluPol_C-huANP32A and FluPol_C-chANP32A complexes.

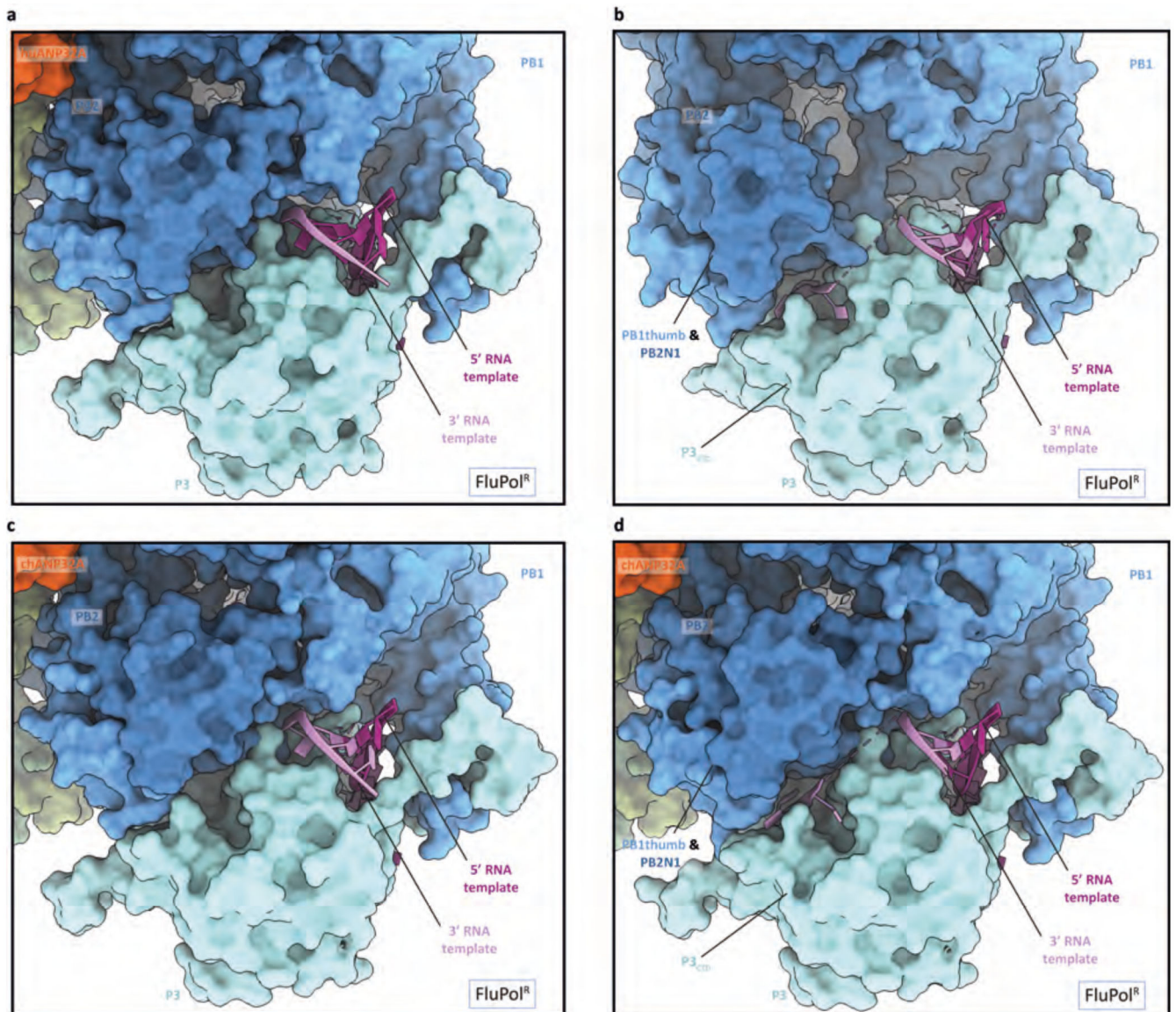
a, e, Representative micrograph of FluPol_C-huANP32A (**a**) and FluPol_C-chANP32A (**e**) embedded in vitreous ice. Scale bar, 200 Å. **b, f**, Representative 2D class averages of FluPol_C-huANP32A (**b**) and FluPol_C-chANP32A (**f**). **c, d**, Data analysis for FluPol_C-huANP32A Subclass1 (**c**) and Subclass2 (**d**). 3D reconstruction locally filtered and coloured according to RELION local resolution (left panel). FSC curve indicating overall map resolution and model-to-map FSC (middle panel). Curves are shown for phase

randomisation, unmasked, masked and phase-randomisation-corrected masked maps. Angular distribution of particle projections with the cryo-EM map shown in grey (right panel). **g-j**, Data analysis for FluPol_C-chANP32A Subclass1 (**g**), Subclass2 (**h**), Subclass3 (**i**) and Subclass4 (**j**). 3D reconstruction locally filtered and coloured according to RELION local resolution (top panel). FSC curve indicating overall map resolution and the model-to-map FSC (middle panel). Curves are shown for phase randomisation, unmasked, masked and phase-randomisation-corrected masked maps. Angular distribution of particle projections with the cryo-EM map shown in grey (bottom panel).

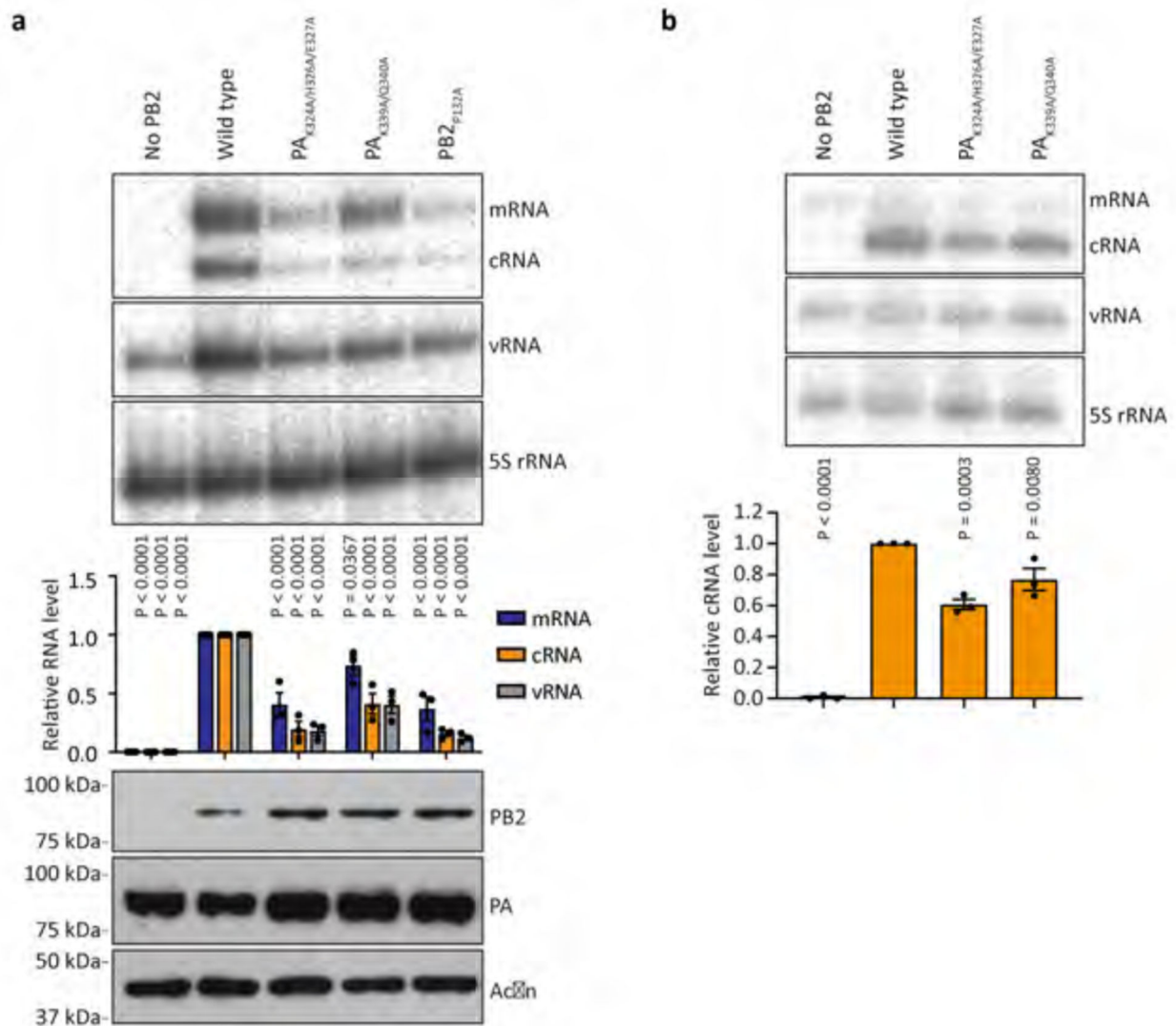


Extended Data Fig. 4. Comparison of FluPol^R and FluPol^E structures with the transcriptase and apo conformations of FluPol.

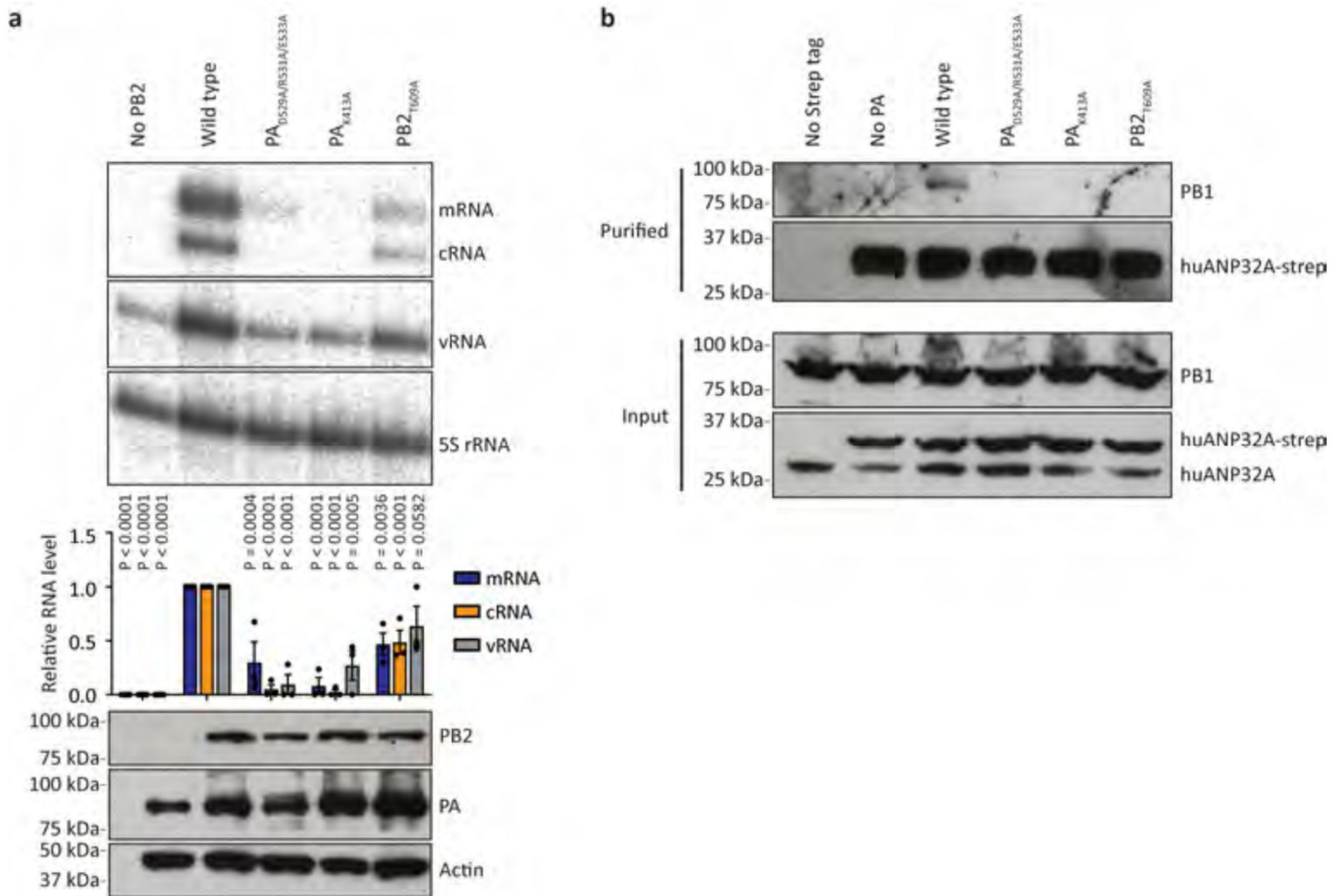
a-d, Comparison of structures of human influenza A/NT/60/68 (H3N2) bound to vRNA and capped RNA in the transcriptase conformation (PDB: 6RR7) (**a**) and human influenza C/Johannesburg/1/66 in the apo conformation (PDB: 5D98) (**b**) with structures of FluPol^R (**c**) and FluPol^E (**d**) in the FluPol_C-chANP32A complex. **e-h**, Comparison of the PB2 domain arrangements in the complexes shown in **a-d**.



Extended Data Fig. 5. Close-up view of the interaction of 5' and 3' vRNA termini with FluPol^R.
a, c, Close-up view of the 3' vRNA pointing towards the active site in the FluPol_C-huANP32A (**a**) and FluPol_C-chANP32A (**c**) structures. **b, d,** Close-up view of the 3' vRNA binding in a groove located between P3_{CTD} and the PB1_{thumb} and PB2_{N1} subdomains in the FluPol_C-huANP32A (**b**) and FluPol_C-chANP32A (**d**) structures.

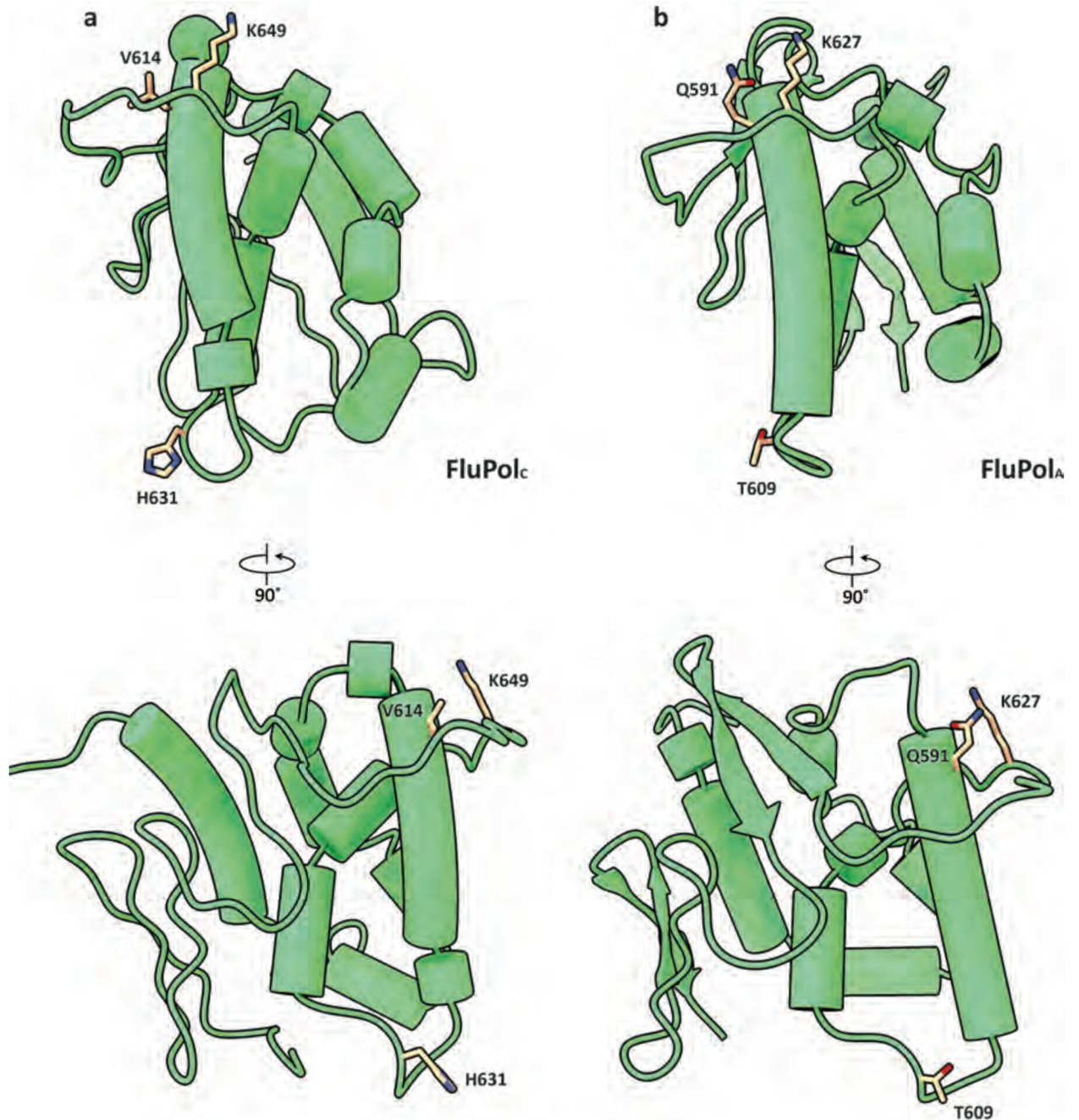


Extended Data Fig. 6. Effect of FluPol^R-FluPol^E dimer interface mutations on FluPol_A activity.
a, b, Effect of mutations at the FluPol^R-FluPol^E dimer interface on FluPol_A activity in viral minigenome assays (**a**) and cRNA encapsidation by FluPol_A (**b**). Data are presented as mean values \pm s.e.m. $n = 3$ biologically independent samples from $n = 3$ independent experiments. Ordinary one-way ANOVA with Dunnett's post hoc test for multiple comparisons. $P < 0.05$ is considered significant to reject the null hypothesis. Western blot analyses were repeated from $n = 3$ independent experiments with similar results. For gel source data, see Supplementary Fig. 2.



Extended Data Fig. 7. Effect of FluPol_A mutations at the FluPol_A-ANP32A interface on FluPol_A activity and interaction with huANP32A.

a, b, Effect of FluPol_A mutations at the FluPol_A-ANP32A interface on FluPol_A activity in viral minigenome assays on (a) and FluPol_A-ANP32A interaction (b). Data are presented as mean values ± s.e.m. $n = 3$ biologically independent samples from $n = 3$ independent experiments. Ordinary one-way ANOVA with Dunnett's post hoc test for multiple comparisons. $P < 0.05$ is considered significant to reject the null hypothesis. Western blot analyses were repeated from $n = 3$ independent experiments with similar results. For gel source data, see Supplementary Fig. 2.



Extended Data Fig. 8. Structural comparison of PB2₆₂₇ domains of FluPol_A and FluPol_C. Structures of the PB2₆₂₇ domains from crystal structures of FluPol from influenza C/ Johannesburg/1/1966 (a, PDB ID: 5D98) and A/NT/60/1968 (H3N2) (b, PDB ID: 6QNW) viruses are aligned and shown in cartoon mode. Residues discussed in this study are highlighted in stick mode and coloured in orange.

Extended Data Table 1
Cryo-EM data collection, refinement and validation
statistics

	FluPol _c -huANP32			FluPol _c -chANP32		
	Sub-Class1 EMD-10665 6XZQ	Sub-Class2 EMD-10667 6YOC	Sub-Class1 EMD-10666 6XZR	Sub-Class2 EMD-10659 6XZQ	Sub-Class3 EMD-10662 6XZG	Sub-Class4 EMD-10664 6XZR
Data collection						
Microscope	Titan Krios IV (eBIC)			Titan Krios (Strubi)		
Voltage (kV)	300			300		
Detector	Gatan K3 with EF			Gatan K2 with EF		
Recording mode	Super Resolution			Counting		
Magnification	81,000			105,000		
Movie/micrograph pixel size (Å)	0.5425			1.37		
Dose rate (e-/Å ² / sec)	16			3.53		
Number of frames per movie	30			44		
Movie exposure time (s)	2			11		
Total dose (e-/Å ²)	32.1			38.8		
Defocus range (um)	2 to -3.5			-2 to -3.5		
Volta Phase Plate	no			no		
EM data processing						
Number of movies/ micrographs	9287			3678		
Box size (px)	300	450		280		
Particle number (total)	2,312,045			2,534,332		
Particle number (post 2D)	846,766			875,856		
Particle number (post 3D)	835,000			773,000		
Particle number (used in final map)	85,000	57,000	349K	169K	77K	71K
Symmetry	C1	C1	C1	C1	C1	C1
Map resolution (FSC 0.143)	3.6	3.2	3.3	3.4	3.8	3.3
Local resolution range (FSC 0.5)	3.3-5.7	3.1-4.7	3.1-5.7	3.1-4.7	3.5-5.9	3.3-5.7
Map sharpening B- factor (Å ²)	-35	-30	-65	-105	-65	-90
Model Building and Validation						
Initial model used	6XZR	6XZR	5D98, 6RR7, 4XOS	6XZR	6XZR	6XZR
Model composition						
Non-hydrogen protein atoms	56895	34969	66214	63743	66001	66227

	FluPol _C -huANP32			FluPol _C -chANP32		
	Sub-Class1 EMD-10665 6XZQ	Sub-Class2 EMD-10667 6Y0C	Sub-Class1 EMD-10666 6XZR	Sub-Class2 EMD-10659 6XZQ	Sub-Class3 EMD-10662 6XZG	Sub-Class4 EMD-10664 6XZR
Protein residues	3492	2135	4077	3919	4065	4077
Nucleotides (RNA)	19	20	19	20	19	20
RMSD from ideal						
Bond length (Å)	0.005	0.006	0.006	0.003	0.005	0.005
Bond angles (°)	0.638	0.679	0.576	0.53	0.695	0.749
Validation						
Molprobrity score	1.74	1.96	1.74	1.82	1.82	1.87
Clashscore	5.76	6.1	6.47	7.81	7.75	8.67
Rotamers outliers (%)	1.26	2.2	0.83	0.26	0.92	0.17
FSC (0.5) model- vs-map	3.63	3.68	3.3	3.45	3.73	3.55
CC model-vs-map (masked)	0.73	0.76	0.81	0.75	0.78	0.78
Ramachandran plot						
Favored(%)	95	94.84	94.32	94.27	94.12	93.92
Allowed (%)	5	5.16	5.68	5.73	5.88	6.08
Outliers (%)	0	0	0	0	0	0

Supplementary Material

Refer to Web version on PubMed Central for supplementary material.

Acknowledgements

We thank N. Naffakh, P-C. Shaw, G.G. Brownlee, F. Vreede for plasmids, I. Berger for the MultiBac system. We thank D. Karia, A. Howe and D. Clare for assistance with cryo-EM. We thank G.G. Brownlee, D. Stuart, as well as members of the Fodor and Grimes laboratories, for helpful comments and discussions. This work was supported by Medical Research Council (MRC) programme grant MR/R009945/1 (to E.F.), Wellcome Investigator Awards 200835/Z/16/Z (to J.M.G.) and 205100/Z/16/Z (to W.S.B.), MRC Studentship (to A.P.W.) and Imperial College President's PhD Scholarship (to E.S.). The authors would like to thank Diamond Light source for access and support of the cryo-EM facilities at the UK national Electron Bio-Imaging Centre (eBIC) (proposal EM20223), funded by the Wellcome, MRC and BBSRC. Further EM provision was provided through the OPIC electron microscopy facility which was founded by a Wellcome JIF award (060208/Z/00/Z) and is supported by a Wellcome equipment grant (093305/Z/10/Z). Computation used the Oxford Biomedical Research Computing (BMRC) facility, a joint development between the Wellcome Centre for Human Genetics and the Big Data Institute supported by Health Data Research UK and the NIHR Oxford Biomedical Research Centre. The views expressed are those of the author(s) and not necessarily those of the NHS, the NIHR or the Department of Health. Part of this work was supported by Wellcome administrative support grant (203141/Z/16/Z).

Data availability

All data are available from the corresponding authors and/or included in the manuscript or Supplementary Information. Cryo-EM density maps with the corresponding atomic coordinates have been deposited in the Electron Microscopy Data Bank and the Protein Data Bank, respectively, with accession codes EMD-10665, PDB ID 6XZQ (FluPol_C-huANP32A-subclass 1), EMD-10667, PDB ID 6Y0C (FluPol_C-huANP32A-subclass 2), EMD-10666,

PDB ID 6XZR (FluPol_C-chANP32A-subclass 1), EMD-10659, PDB ID 6XZD (FluPol_C-chANP32A-subclass 2), EMD-10662, PDB ID 6XZG (FluPol_C-chANP32A-subclass 3), EMD-10664, PDB ID 6XZP (FluPol_C-chANP32A-subclass 4).

References

1. Krammer F, et al. Influenza. *Nat Rev Dis Primers*. 2018; 4:3. [PubMed: 29955068]
2. Fodor E, Te Velthuis AJW. Structure and Function of the Influenza Virus Transcription and Replication Machinery. *Cold Spring Harb Perspect Med*. 2019
3. Wandzik JM, Kouba T, Cusack S. Structure and Function of Influenza Polymerase. *Cold Spring Harb Perspect Med*. 2020
4. Long JS, et al. Species difference in ANP32A underlies influenza A virus polymerase host restriction. *Nature*. 2016; 529:101–4. [PubMed: 26738596]
5. Walker AP, Fodor E. Interplay between Influenza Virus and the Host RNA Polymerase II Transcriptional Machinery. *Trends Microbiol*. 2019; 27:398–407. [PubMed: 30642766]
6. Peacock TP, Sheppard CM, Staller E, Barclay WS. Host Determinants of Influenza RNA Synthesis. *Annu Rev Virol*. 2019; 6:215–233. [PubMed: 31283439]
7. Staller E, et al. ANP32 Proteins Are Essential for Influenza Virus Replication in Human Cells. *J Virol*. 2019:93.
8. Zhang H, et al. Fundamental Contribution and Host Range Determination of ANP32A and ANP32B in Influenza A Virus Polymerase Activity. *J Virol*. 2019:93.
9. Huyton T, Wolberger C. The crystal structure of the tumor suppressor protein pp32 (Anp32a): structural insights into Anp32 family of proteins. *Protein Sci*. 2007; 16:1308–15. [PubMed: 17567741]
10. Hengrung N, et al. Crystal structure of the RNA-dependent RNA polymerase from influenza C virus. *Nature*. 2015; 527:114–7. [PubMed: 26503046]
11. Thierry E, et al. Influenza Polymerase Can Adopt an Alternative Configuration Involving a Radical Repacking of PB2 Domains. *Mol Cell*. 2016; 61:125–37. [PubMed: 26711008]
12. Fan H, et al. Structures of influenza A virus RNA polymerase offer insight into viral genome replication. *Nature*. 2019; 573:287–290. [PubMed: 31485076]
13. Pflug A, Guilligay D, Reich S, Cusack S. Structure of influenza A polymerase bound to the viral RNA promoter. *Nature*. 2014; 516:355–60. [PubMed: 25409142]
14. Peng Q, et al. Structural insight into RNA synthesis by influenza D polymerase. *Nat Microbiol*. 2019; 4:1750–1759. [PubMed: 31209309]
15. Wandzik JM, et al. A Structure-Based Model for the Complete Transcription Cycle of Influenza Polymerase. *Cell*. 2020; 181:877–893. [PubMed: 32304664]
16. Chang S, et al. Cryo-EM structure of influenza virus RNA polymerase complex at 4.3 Å resolution. *Mol Cell*. 2015; 57:925–935. [PubMed: 25620561]
17. Long JS, et al. Species specific differences in use of ANP32 proteins by influenza A virus. *Elife*. 2019:8.
18. Bi Z, et al. Insights into species-specific regulation of ANP32A on the mammalian-restricted influenza virus polymerase activity. *Emerg Microbes Infect*. 2019; 8:1465–1478. [PubMed: 31608791]
19. Zhang H, et al. A unique feature of swine ANP32A provides susceptibility to avian influenza virus infection in pigs. *PLoS Pathog*. 2020; 16:e1008330. [PubMed: 32084248]
20. Baker SF, Ledwith MP, Mehle A. Differential Splicing of ANP32A in Birds Alters Its Ability to Stimulate RNA Synthesis by Restricted Influenza Polymerase. *Cell Rep*. 2018; 24:2581–2588. [PubMed: 30184493]
21. Camacho-Zarco AR, et al. Molecular basis of host-adaptation interactions between influenza virus polymerase PB2 subunit and ANP32A. *Nat Commun*. 2020; 11
22. Mistry B, et al. Elucidating the Interactions between Influenza Virus Polymerase and Host Factor ANP32A. *J Virol*. 2020:94.

23. Domingues P, Hale BG. Functional Insights into ANP32A-Dependent Influenza A Virus Polymerase Host Restriction. *Cell Rep.* 2017; 20:2538–2546. [PubMed: 28903035]
24. Mehle A, Doudna JA. Adaptive strategies of the influenza virus polymerase for replication in humans. *Proc Natl Acad Sci U S A.* 2009; 106:21312–6. [PubMed: 19995968]
25. Yamada S, et al. Biological and structural characterization of a host-adapting amino acid in influenza virus. *PLoS Pathog.* 2010; 6:e1001034. [PubMed: 20700447]
26. Chin AWH, et al. Influenza A viruses with different amino acid residues at PB2-627 display distinct replication properties in vitro and in vivo: revealing the sequence plasticity of PB2627 position. *Virology.* 2014; 468-470:545–555. [PubMed: 25262472]
27. Vreede FT, Jung TE, Brownlee GG. Model suggesting that replication of influenza virus is regulated by stabilization of replicative intermediates. *J Virol.* 2004; 78:9568–72. [PubMed: 15308750]
28. Nilsson BE, Te Velthuis AJW, Fodor E. Role of the PB2 627 Domain in Influenza A Virus Polymerase Function. *J Virol.* 2017:91.
29. Manz B, Brunotte L, Reuther P, Schwemmle M. Adaptive mutations in NEP compensate for defective H5N1 RNA replication in cultured human cells. *Nat Commun.* 2012; 3
30. Sugiyama K, Kawaguchi A, Okuwaki M, Nagata K. pp32 and APRIL are host cell-derived regulators of influenza virus RNA synthesis from cRNA. *Elife.* 2015:4.
31. Pan J, et al. Structure of the human metapneumovirus polymerase phosphoprotein complex. *Nature.* 2020; 577:275–279. [PubMed: 31698413]
32. Lukarska M, et al. Structural basis of an essential interaction between influenza polymerase and Pol II CTD. *Nature.* 2017; 541:117–121. [PubMed: 28002402]
33. Serna Martin I, et al. A Mechanism for the Activation of the Influenza Virus Transcriptase. *Mol Cell.* 2018; 70:1101–1110. [PubMed: 29910112]
34. Chen KY, Santos Afonso ED, Enouf V, Isel C, Naffakh N. Influenza virus polymerase subunits co-evolve to ensure proper levels of dimerization of the heterotrimer. *PLoS Pathog.* 2019; 15:e1008034. [PubMed: 31581279]
35. Killip MJ, Fodor E, Randall RE. Influenza virus activation of the interferon system. *Virus Res.* 2015; 209:11–22. [PubMed: 25678267]
36. Bieniossek C, Imasaki T, Takagi Y, Berger I. MultiBac: expanding the research toolbox for multiprotein complexes. *Trends in Biochemical Sciences.* 2012; 37:49–57. [PubMed: 22154230]
37. Zheng SQ, et al. MotionCor2: anisotropic correction of beam-induced motion for improved cryo-electron microscopy. *Nat Methods.* 2017; 14:331–332. [PubMed: 28250466]
38. Zhang K. Gctf: Real-time CTF determination and correction. *J Struct Biol.* 2016; 193:1–12. [PubMed: 26592709]
39. Punjani A, Rubinstein JL, Fleet DJ, Brubaker MA. cryoSPARC: algorithms for rapid unsupervised cryo-EM structure determination. *Nat Methods.* 2017; 14:290–296. [PubMed: 28165473]
40. Scheres SH. RELION: implementation of a Bayesian approach to cryo-EM structure determination. *J Struct Biol.* 2012; 180:519–30. [PubMed: 23000701]
41. Naydenova K, Russo CJ. Measuring the effects of particle orientation to improve the efficiency of electron cryomicroscopy. *Nat Commun.* 2017; 8
42. Tan YZ, et al. Addressing preferred specimen orientation in single-particle cryo-EM through tilting. *Nat Methods.* 2017; 14:793–796. [PubMed: 28671674]
43. Pettersen EF, et al. UCSF Chimera--a visualization system for exploratory research and analysis. *J Comput Chem.* 2004; 25:1605–12. [PubMed: 15264254]
44. Emsley P, Lohkamp B, Scott WG, Cowtan K. Features and development of Coot. *Acta Crystallogr D Biol Crystallogr.* 2010; 66:486–501. [PubMed: 20383002]
45. Jakobi AJ, Wilmanns M, Sachse C. Model-based local density sharpening of cryo-EM maps. *Elife.* 2017; 6
46. Burnley T. Introducing the Proceedings of the CCP-EM Spring Symposium. *Acta Crystallogr D Struct Biol.* 2017; 73:467–468. [PubMed: 28580907]
47. Adams PD, et al. PHENIX: a comprehensive Python-based system for macromolecular structure solution. *Acta Crystallographica Section D-Biological Crystallography.* 2010; 66:213–221.

48. Davis IW, et al. MolProbity: all-atom contacts and structure validation for proteins and nucleic acids. *Nucleic Acids Res.* 2007; 35:W375–83. [PubMed: 17452350]
49. Waterhouse A, et al. SWISS-MODEL: homology modelling of protein structures and complexes. *Nucleic Acids Res.* 2018; 46:W296–W303. [PubMed: 29788355]
50. Crescenzo-Chaigne B, Naffakh N, van der Werf S. Comparative analysis of the ability of the polymerase complexes of influenza viruses type A, B and C to assemble into functional RNPs that allow expression and replication of heterotypic model RNA templates in vivo. *Virology.* 1999; 265:342–53. [PubMed: 10600605]
51. Tang YS, Lo CY, Mok CK, Chan PK, Shaw PC. The Extended C-Terminal Region of Influenza C Virus Nucleoprotein Is Important for Nuclear Import and Ribonucleoprotein Activity. *J Virol.* 2019; 93
52. Fodor E, et al. A single amino acid mutation in the PA subunit of the influenza virus RNA polymerase inhibits endonucleolytic cleavage of capped RNAs. *J Virol.* 2002; 76:8989–9001. [PubMed: 12186883]
53. Fodor E, et al. Rescue of influenza A virus from recombinant DNA. *J Virol.* 1999; 73:9679–82. [PubMed: 10516084]
54. Paterson D, te Velthuis AJ, Vreede FT, Fodor E. Host restriction of influenza virus polymerase activity by PB2 627E is diminished on short viral templates in a nucleoprotein-independent manner. *J Virol.* 2014; 88:339–44. [PubMed: 24155385]
55. Robb NC, Smith M, Vreede FT, Fodor E. NS2/NEP protein regulates transcription and replication of the influenza virus RNA genome. *J Gen Virol.* 2009; 90:1398–407. [PubMed: 19264657]
56. Deng T, et al. Role of ran binding protein 5 in nuclear import and assembly of the influenza virus RNA polymerase complex. *J Virol.* 2006; 80:11911–9. [PubMed: 17005651]
57. Vreede FT, Brownlee GG. Influenza virion-derived viral ribonucleoproteins synthesize both mRNA and cRNA in vitro. *J Virol.* 2007; 81:2196–204. [PubMed: 17166911]
58. Schneider CA, Rasband WS, Eliceiri KW. NIH Image to ImageJ: 25 years of image analysis. *Nat Methods.* 2012; 9:671–5. [PubMed: 22930834]
59. Engelhardt OG, Smith M, Fodor E. Association of the influenza A virus RNA-dependent RNA polymerase with cellular RNA polymerase II. *J Virol.* 2005; 79:5812–8. [PubMed: 15827195]
60. Robert X, Gouet P. Deciphering key features in protein structures with the new ENDscript server. *Nucleic Acids Res.* 2014; 42:W320–4. [PubMed: 24753421]

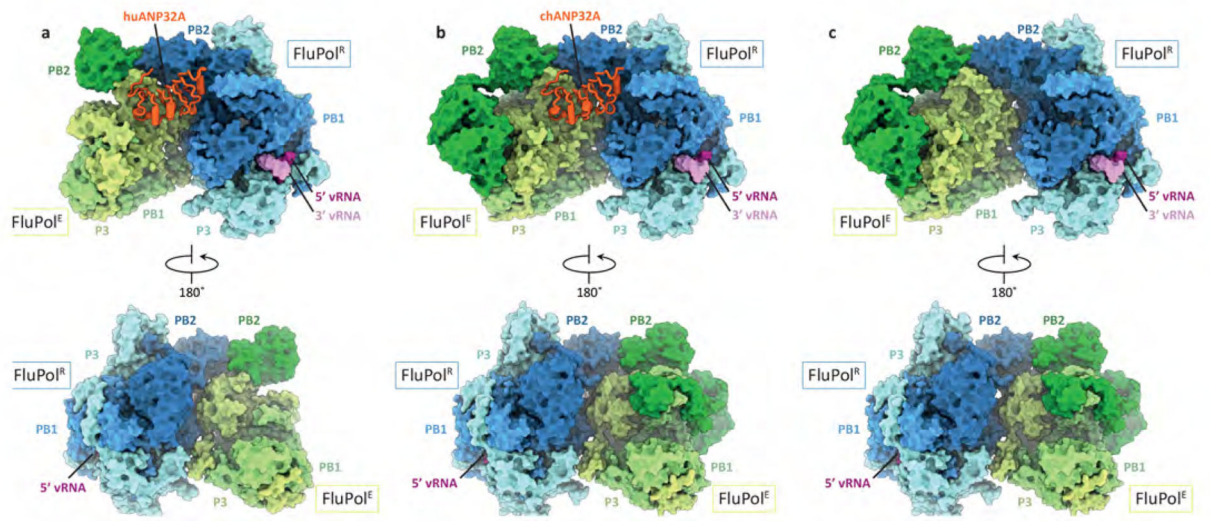


Fig. 1. Structures of dimers of FluPol_C heterotrimers with or without bound ANP32A.
a-c, Cryo-EM structures of dimers of FluPol_C heterotrimers bound to huANP32A (a),
 chANP32A (b), and without ANP32A (c).

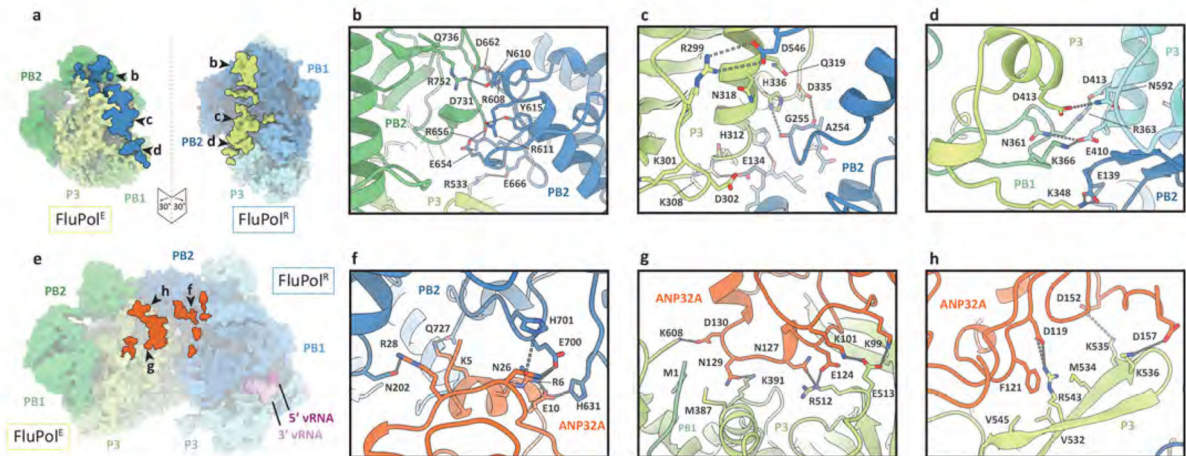


Fig. 2. FluPol_C-FluPol_C and ANP32A-FluPol_C interaction interfaces.

a, FluPol_C-FluPol_C dimer interface with interacting regions in FluPol^R and FluPol^E highlighted on the molecular surface, by peeling apart the two molecules each by 30°. The letters denote the close-up views shown in panels **b-d**, Close-up views of the FluPol_C-FluPol_C interaction interface. Dashed lines indicate hydrogen bonds. **e**, ANP32A-FluPol_C surface interface with interacting regions in FluPol_C highlighted. The letters denote the close-up views shown in panels **f-h**, Close-up views of the ANP32A-FluPol_C interaction interface. Dashed lines indicate hydrogen bonds.

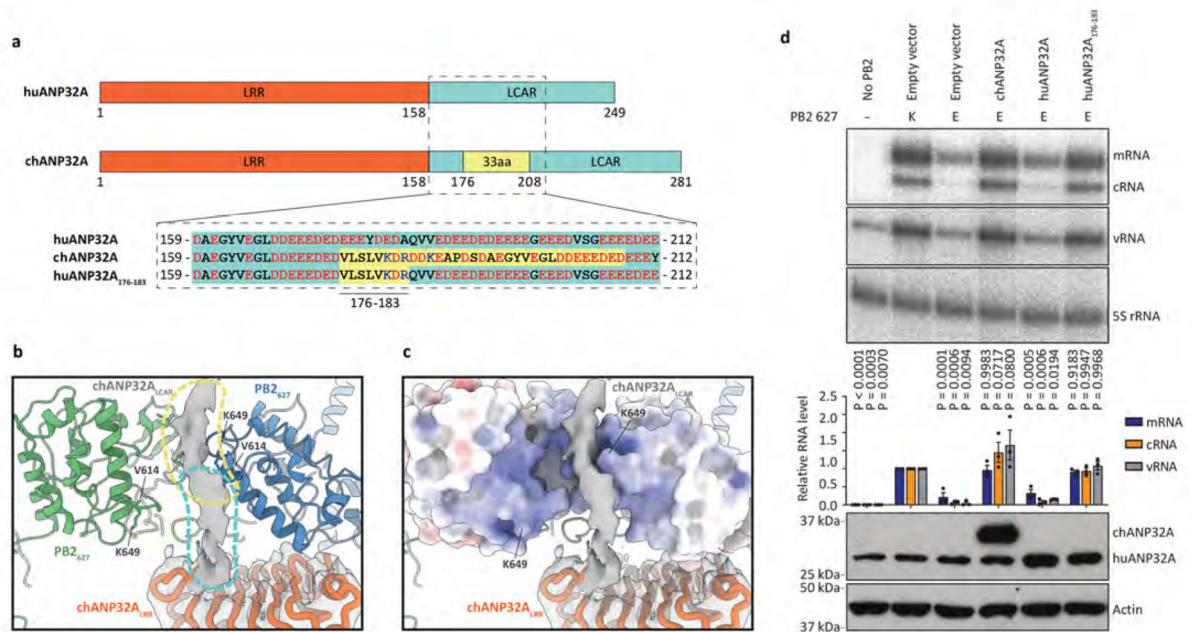


Fig. 3. Interaction of ANP32_{LCAR} with FluPol_C and the effect of ANP32A on FluPol_A activity.

a, Schematic of huANP32A and chANP32A highlighting the 33 amino acid (33 aa) insertion in chANP32A and sequence differences. **b**, Close-up view of the cryo-EM density attributed to chANP32A (grey, threshold 0.934) with the chANP32A_{LRR} domain represented in cartoon (orange) and the positions of PB2₆₂₇ of FluPol^R (blue) and FluPol^E (green). Regions potentially corresponding to the N-terminal part of ANP32A_{LCAR} and part of the avian 33 aa insertion are highlighted in cyan and yellow, respectively. V614 and K649 in FluPol_C corresponds to K/Q591 and K/E627 in FluPol_A, respectively. **c**, Same view as shown in (b), with the PB2₆₂₇ of FluPol^R and FluPol^E shown in surface representation. **d**, Effect of chANP32A and huANP32A, wild type or mutant (huANP32A₁₇₆₋₁₈₃), on the activity of FluPol_A with mammalian-adapted PB2 K627 or avian-signature PB2 E627 in a viral RNP reconstitution assay in mammalian HEK 293T cells. Data of primer extension analysis of viral RNA levels with quantitation (upper panels) and western blot analysis of ANP32A levels (lower panel) with molecular weight markers is shown. Data are presented as mean values \pm s.e.m. $n = 3$ biologically independent samples from $n = 3$ independent experiments. Ordinary one-way ANOVA with Dunnett's post hoc test for multiple comparisons. $P < 0.05$ is considered significant to reject the null hypothesis. Western blot analyses were repeated from $n = 3$ independent experiments with similar results. For gel source data, see Supplementary Fig. 2.

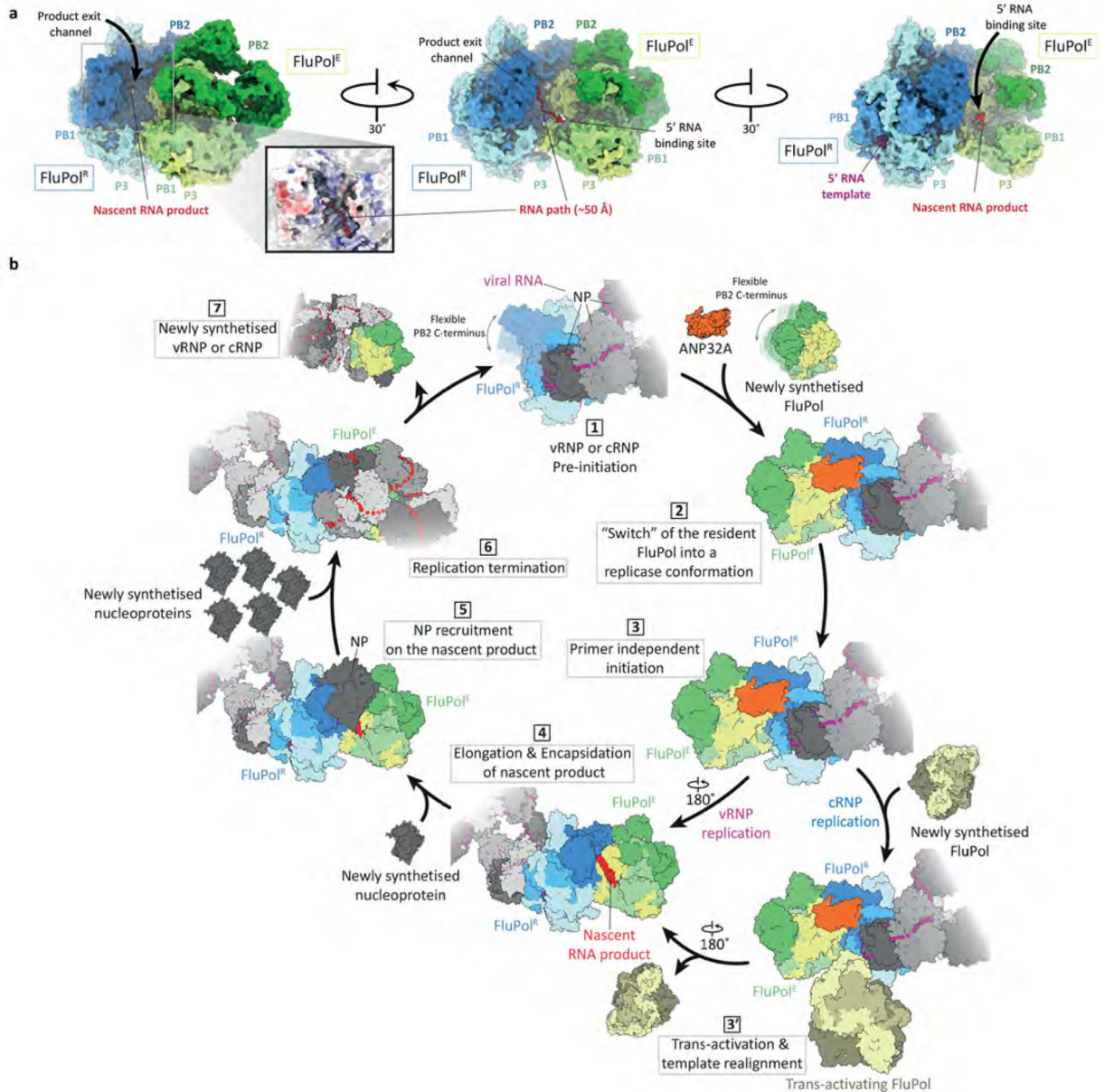


Fig. 4. Functional implications of the FluPol_C-ANP32A complex.

a, Relative positions of the RNA product exit channel in FluPol^R and the 5' RNA binding site in FluPol^E in the chANP32A-FluPol_C complex. The positions of the RNA product exit channel in FluPol^R and the 5' RNA binding site in FluPol^E were determined by superposing FluPol^R and FluPol^E with the structure of FluPol_A bound to capped RNA and vRNA template (PDB 6RR7). **b**, Model for the role of FluPol-ANP32A complex in the replication of the influenza virus RNA genome and its assembly into RNP. FluPol in the context of vRNP or cRNP is flexible (1) but is stabilised in a replicase FluPol^R conformation upon binding of a newly synthesised FluPol in the presence of ANP32A (2). FluPol^R initiates replication in a primer independent manner (3) with a trans-activating FluPol involved in

cRNA to vRNA replication by promoting cRNA template realignment (3'). As the 5' end of the nascent replication product is released from the polymerisation active site of FluPol^R, it is captured in the 5' RNA binding pocket of the encapsidating FluPol^E bound to FluPol^R (4), initiating the encapsidation of the nascent RNA with NP (5). Nascent vRNA or cRNA assemble into vRNP or cRNP, respectively (6), and are released upon FluPol^R termination. FluPol^E becomes the resident polymerase of the newly produced vRNP or cRNP.